An Atomically Resolved Schottky Barrier Height Approach for Bridging the Gap between Theory and Experiment at Metal-Semiconductor Heterojunctions

Viacheslav Sorkin[1,*,#], Hangbo Zhou[1], Zhi Gen Yu[1], Kah-Wee Ang[2], Yong-Wei Zhang[1,#],

[1] Institute of High Performance Computing (IHPC), Agency for Science, Technology and Research (A*STAR) 1 Fusionopolis Way, #16-16 Connexis, Singapore 138632, Republic of Singapore.

[2] Department of Electrical and Computer Engineering National University of Singapore 4 Engineering Drive 3, Singapore 117583, Republic of Singapore.

Co-corresponding authors: sorkinv@ihpc.a-star.edu.sg, zhangyw@ihpc.a-star.edu.sg

Abstract

We propose an atomically resolved approach to capture the spatial variations of Schottky barrier height (SBH) at metal-semiconductor heterojunctions. This proposed scheme, based on atom-specific partial density of states (PDOS) calculations, further enables the calculation of the effective SBH that aligns with conductance measurements. We apply this approach to study the variations of SBH at MoS_2@Au heterojunctions, in which MoS_2 contains conducting and semiconducting grain boundaries (GBs). Our results reveal that there are significant variations in SBH at atoms in the defected heterojunctions. Of particular interest is the fact that the SBH in some areas with extended defects approaches zero, indicating Ohmic contact. One important implication of this finding is that the effective SBH should be intrinsically dependent on the defect density and character. Remarkably, the obtained effective SBH values demonstrate a good agreement with existing experimental measurements. Thus, the present study addresses two long-standing challenges associated with SBH in MoS_2-metal heterojunctions: the wide variation in experimentally measured SBH values at MoS_2@metal heterojunctions and the large discrepancy between density-functional-theory-predicted and experimentally measured SBH values. Our proposed approach points out a valuable pathway for understanding and manipulating SBHs at metal-semiconductor heterojunctions.

Keywords: atomically resolved SBH, effective SBH, spatial variation in SBH, GBs, edge dislocations

Introduction

Schottky barrier height (SBH) is a critical parameter at metal-semiconductor heterojunctions, playing a pivotal role in the performance of electronic devices. SBH acts as a gatekeeper for current in metal-semiconductor junctions. A higher SBH translates to a lower electrical conduction at the heterojunction, thus affecting the switching speed in transistors and memristors. By manipulating SBH, engineers can tailor devices for specific applications[1–3]. Accurate determination of SBH values is essential for optimizing device functionality and design. However, the field of SBH characterization has long grappled with two significant challenges. Firstly, there is a wide variation in experimentally measured SBH values at metal-semiconductor heterojunctions. Secondly, there has been a persistent discrepancy between SBH values predicted through density functional theory (DFT) and those

obtained from experimental measurements. For example, the experimental measurements of the SBH in MoS_2@Au heterojunctions reported a widespread range of SBH values from 0.2 eV to 0.9 eV[4–8]. In addition, density functional theory (DFT) calculations predict a relatively narrow range of values from 0.6 eV to 0.8 eV[8–14], generally overestimating the experimental measurements. The large variations in the experimental measurements have been attributed to various factors, including the preparation method, the quality of the interface, and the presence of defects, and the overestimation of the theoretical calculations has been also attributed to various factors, including Fermi-level (FL) pinning[8,15–18], band misalignment[19,20], charge redistribution[21,22], interface dipole formation[23,24], push-back effect[16,25], interfacial stress and strain[26,27], and defects[11,22,27–31]. Clearly, the underlying origins responsible for these challenges remain unclear. Therefore, addressing these challenges becomes an imperative task.

Here, we utilize MoS_2-metal heterojunctions as an example to illustrate our approach in addressing these challenges, bearing in mind that our approach is applicable to any metal-semiconductor heterojunctions. An appealing reason for choosing MoS_2 is that it is a two-dimensional material promising for the next-generation nanoelectronics, such as artificial synapses, bio-sensors, memristors, and digital memory storage[27,32–38]. MoS_2 stands out as a promising material for future nanoelectronics due to its unique properties [1]. Unlike graphene, it possesses a tunable direct bandgap ideal for optoelectronics. Additionally, MoS_2 exhibits a high carrier mobility, high on/off ratio of up to 10^8, and the ability to switch resistance states, making it suitable for advanced transistors and logic devices[1,2,35]. The compatibility of MoS_2 with existing fabrication techniques, coupled with its environmental stability, makes it a strong contender for next-generation devices. Progress in development of these devices relies on breakthroughs in both synthesis of two-dimensional materials[39–41] and design of device architectures[19,32,42,43]. Precise control of the SBH at MoS_2-metal interface is essential for the development of these devices[44].

On one hand, traditionally, the electrical property at the metal-semiconductor heterojunctions is assumed to be uniform, conventionally characterized by a single physical quantity, SBH. A good example is the DFT methods for calculating the SBH at the MoS_2@metal interface. Two DFT-based approaches are commonly used to compute SBH. The first one involves aligning the electronic band structure of the contact MoS_2 monolayer extracted from the MoS_2@metal heterojunction with the heterojunction itself to identify the conduction band minimum (CBM) of the metal-supported MoS_2 layer. The SBH is obtained as the energy difference between the FL and the identified CBM[12,16,45,46]. In this method, PDOS of Mo and S atoms in the MoS_2@metal monolayer are used to identify the SBH[11,27]. The second one is based on the Schottky-Mott (SM) rule[20], which predicts the SBH according to the difference between metal work function and MoS_2 electron affinity. The extended SM rule incorporates metal-MoS_2 interactions via the Hartree potential[12,46]. In these calculation approaches, the interface is assumed to be spatially uniform[32,47,48], and the SBH is, implicitly, obtained by averaging over all the atoms.

On the other hand, atomically resolved measurements, such as scanning tunnelling microscope (STM) and scanning tunnelling spectroscopy (STS), clearly demonstrate the large SBH variations across the MoS2-metal interface[47]. It is understood that STM indirectly probes SBH by mapping surface potential and inferring SBH spatial variations[48]. Hence, it measures the current through atomic-scale junctions, and thus reveals the local SBH variations. Similarly, STS also probes the local electronic density of states, providing insights into SBH dependence on atomic arrangements. Clearly, those STM and STS measurements provide qualitative insights into the non-uniform SBH landscape, highlighting the cruciality for considering the variations in SBHs across the metal-semiconductor interface.

Our above analysis clearly pinpoints the fundamental difference in obtaining the SBH between the experimental measurements and theoretical treatments. It is noted that the simplified approach used in the theoretical treatments may be valid for a defect-free interface , however, it may fail to capture the inhomogeneities inherent in real MoS_2@metal heterojunctions due to the presence of defects, impurities, interface states, and other factors[11,25,49]. Our hypothesis is that it is this uniformity assumption for the interfaces that leads to the discrepancies between the experiments and the theories and the large variations in the experimental measurements.

In response to these challenges, this paper introduces an atomically resolved methodology for investigating the spatial variations of SBH at metal-semiconductor heterojunctions. This new approach is based on atom-specific PDOS calculations, offering the ability to calculate atomically resolved SBH values and, from which we derived effective overall SBH values in non-uniform interfaces. Our research focuses on MoS2@metal heterojunctions, with a specific examination of conducting and semiconducting grain boundaries (GBs) within these structures. Through our study, we uncover that extended defects, such as grain boundaries, have a substantial impact on the effective SBH, which would be otherwise missing in the traditional approach. The effective SBH values obtained through our novel approach exhibit remarkable agreement with experimental measurements.

We recognize the remarkable progress in fabricating high-quality, large-area MoS_2 films. However, achieving complete absence of defects across these vast scales remains a significant hurdle[1,50]. Even these advanced films likely contain some GBs, which may impact both the SBH and overall device performance. Our model directly addresses this challenge by incorporating the effects of GBs. This allows us to provide valuable insights into how GBs influence SBH and ultimately, nanoelectronics device behaviour. Furthermore, this work contributes to the broader understanding of how various defects in 2D materials can be modelled and potentially mitigated during device design and optimization[1,50]. By considering these factors, it paves the way for MoS_2 devices with superior performance and reliability in real-world applications.

Additionally, our analysis of the atom-resolved SBH distribution sheds light on the underlying factors responsible for variations in measured SBHs. These findings highlight the critical importance of considering spatial variations in SBH values and advocate for the necessity of atomistic SBH calculations, especially when dealing with defect-rich MoS_2 layers.

Atomically Resolved SBH Theoretical Framework

As discussed in the introduction, the SBH at the metal@MoS_2 interface is traditionally assumed to be uniform, characterized by a single parameter ϕ_B. However, a more accurate representation considers the SBH as a function of spatial position, denoted as $\phi_B(x, y)$, with the z-axis perpendicular to the interface. While the traditional approach may remain valid in periodic lattice, the transition from a uniform SBH to a position-dependent $\phi_B(x, y)$ becomes critical when defects, especially extended defects, are introduced. This is because the defects will break the lattice symmetry and thus enlarge the lattice periodicity that surpassing the electron wavelength, over which the $\phi_B(x, y)$ significantly varies. Using MoS_2@Au as example, wavelength λ can be estimated using the Fermi velocity of gold $v_f \sim 10^6\ m/s$, at which electrons emitted from gold to MoS_2[51], yielding $\lambda = h/m_e v_f \sim 5$ Å.

This value is well above the unit cell size of pristine MoS_2 where $a \sim 3$ Å[28] , So electrons are minimally affected by local SBH variations. This justifies the conventional assumption of uniform SBH for such cases (Figure 1(a)).

However, defects, such as grain boundaries (GBs) formed by edge dislocations[52], with a typical size of $a{\sim}7$ Å, can significantly affect the moving electrons. In such scenarios, where $\lambda{\sim}a$, the variations in $\phi_B(x,y)$ become critical and require a position-dependent $\phi_B(x,y)$ representation (Figure 1(b)).

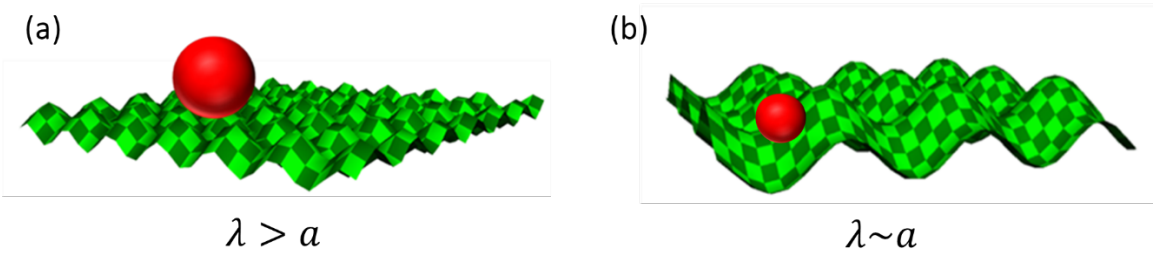

Figure 1: Schematics for atomically resolved SBH for MoS_2-metal interface. *(a) Conventional SBH calculation averaging over the entire interface, which is valid for periodic lattice, when the electron wavelength λ (red) is larger than the variations of SBH at the interface (green), with its periodicity estimated by lattice constant, a: $\lambda > a$. (b) Atomically resolved SBH approach, which is valid for lattice with defects when the electron wavelength λ becomes comparable or larger than a: $\lambda \sim a$, capturing the local variations of SBH at the interface.*

In experiments, the SBH is determined by measuring the current (I) through the MoS_2@metal heterojunction at various voltage biases (V). The thermionic emission theory[4–8] relates I to the SBH, which is determined by integrating the current density across the device area:

$$I = \int_{\text{interface}} dxdy\, j(x,y), \qquad \textit{Eq.1}$$

where $j(x,y)$ is the magnitude of the position-dependent current density vector, assuming that it is perpendicular to the interface. When the electron wavelengths are comparable to local SBH variations $\lambda{\sim}a$, we can evaluate the current density using the thermionic emission model[53], where electrons need sufficient thermal energy to overcome the local $\phi_B(x,y)$ barrier at the interface:

$$j(x,y) = A^*T^2\left(\exp\frac{qV}{k_BT} - 1\right)\exp\left(-\frac{q\phi_B(x,y)}{k_BT}\right), \qquad \textit{Eq.2}$$

where A^* is the effective Richardson constant, V is the voltage bias, k_B is the Boltzmann constant, q is the elementary charge, and T is the temperature.

In standard current measurements, the focus is on the total current flowing through the device rather than the position-dependent current density:

$$I = A^*T^2\left(\exp\frac{qV}{k_BT} - 1\right)\int_{\text{interface}} dxdy\ \exp\left(-\frac{q\phi_B(x,y)}{k_BT}\right) \qquad \textit{Eq.3}$$

In a perfect lattice the SBH is a constant value ϕ_{B0}, then the above equation will reduce to the conventional thermionic emission model. However, for materials with defects and imperfections, the spatial variation of SBH will take effects. In order to restore the thermionic emission formula, we define an effective overall SBH as:

$$\exp\left(-\frac{q\phi_{eff}}{k_BT}\right) = \frac{1}{A}\int_{\text{interface}} dxdy\ \exp\left(-\frac{q\phi_B(x,y)}{k_BT}\right), \qquad \textit{Eq.4}$$

where A is the contact area at the interface measured within the (x,y) plane. With this definition, we can find that the effective SBH can be evaluated as

$$\phi_{eff} = \phi_{B0} - \frac{k_BT}{q}\ln\frac{A_{eff}}{A}, \qquad \textit{Eq 5}$$

where A_{eff} is the effect interfacial area, weighted by the local SBH:

$$A_{eff} = \int_{\text{interface}} dxdy\ \exp\left(-\frac{q[\phi_B(x,y) - \phi_{B0}]}{k_BT}\right)$$

A_{eff} characterize the spatial variation of SBH and it will approach conventional area A when SBH are uniform at interface.

We can find that the second term in *Eq. 5*, caused by the variation of the SBH at the interface, is able to modulate the overall SBH and thus, affects the experimentally measured currents. In tradition approach, this term is not considered by assuming uniformity over the interface[11,12,16,45,46]. However, this oversimplification will overestimate the SBH in materials the variations in the SBH. Thus, a more accurate approach should involve averaging over a Boltzmann-like exponential function (*Eq. 5*), reflecting the dependence of electron transport on local SBH values.

To overcome the limitations of conventional SBH calculations, here, we propose a new approach by defining atomically resolved SBH, ϕ_i, derived from atom-specific PDOS to each atom. This approach assumes that the travelling electrons are associated with specific atoms, essentially experiencing an electron-hopping process[23]. Consequently, the total current arises from the summation of local current at each atom, represented as j_i:

$$I = \int_{\text{interface}} dxdy\, j(x,y) = \sum_{i=all\ atoms} j_i \qquad \textit{Eq.6}$$

where $i \in [1,N]$, N is the number of interfacial atoms.

Based on this concept, the effective SBH can be expressed as:

$$\phi_{eff} = -\frac{k_BT}{q} ln\left(\frac{1}{N}\sum_i^N \exp\left(-\frac{q\phi_i}{k_BT}\right)\right) \qquad \textit{Eq.7}$$

For pristine MoS_2, all the atoms are equivalent, thus, $\phi_i = \phi_{B0}$ for $\forall\ i \in [1,N]$, and the effective SBH (*Eq. 7*) reproduces the SBH value obtained by conventional methods, $\phi_{eff} = \phi_{B0} = \frac{1}{N}\sum_i \phi_i$. This convergence ensures the theoretical consistency by providing a bridge between uniform and non-uniform scenarios.

Admittedly, the weak interaction between MoS_2 and the gold substrate results in the creation of a van der Waals (vdW) gap between them. This gap translates to a significant tunnelling barrier, hindering efficient electron injection from the gold electrode to the MoS_2 monolayer. The tunnelling barrier height (TBH) can be calculated using the plane-averaged electrostatic potential along a direction normal to the MoS_2@Au interface.

SBH and TBH are two distinct concepts with SBH describing the inherent potential jump due to the misalignment between the electron bands of MoS_2 and Au, while TBH reflecting tunnelling difficulty.

A larger TBH due to the vdW gap can effectively increase the perceived SBH for charge carriers. Our model inherently captures this effect. By considering the influence of the vdW gap on the electronic structure and the PDOS functions used to calculate the effective SBH, we implicitly account for the impact of tunnelling difficulty on the apparent barrier height.

In the following, we apply this novel approach to investigate the atomically resolved spatial variations of the SBH at the MoS_2@Au heterojunction with different defective MoS_2 monolayers. We specifically focus on extended defects, particularly edge dislocations with sizes large enough to influence the spatial distribution of the SBH. We considered both conducting and semiconducting GBs formed by these edge dislocations. Due to their prevalence in chemical vapor deposition (CVD) grown MoS_2 and ability to change the SBH, we analyze semiconducting (5|7) armchair (AC) and (4|8) zigzag (ZZ) GBs (Figure 2). Additionally, we also explore conducting mirror GBs, including a (4|4P) GB with four-fold-coordinated S-atoms and a Mo-Mo twin GB with five-fold-coordinated Mo-atoms (Figure 3), demonstrating the applicability of our methodology to diverse GB types with varying electronic properties. We reveal that these heterojunctions exhibit significant SBH variations for the atoms at these extended defects, and such variation of SBH will modulate the overall effective SBH. These modulation of SBH bridges the gap between the computational predictions and experimental measurements.

Computational Model

We investigated the atomic-level SBH variations in a MoS_2@Au heterojunction containing different GBs, including semiconducting GBs for their prevalence, and conducting mirror GBs for highlighting broad applicability of our proposed method. Following the approach of Zou et al.[52], we modelled GBs by introducing equidistant edge dislocations within a periodic simulation cell. This creates a network of infinitely long, rectangular grains with variable widths. Two distinct dreidel-shaped edge dislocations (5|7) and (4|8) were examined for semiconducting GBs[54,55] . Two types of GBs were created: (5|7) GBs formed by (5|7) edge dislocations aligned along the AC direction (Figure 2(a)), and (4|8) GBs formed by (4|8) edge dislocations along ZZ direction (Figure 2(b)).

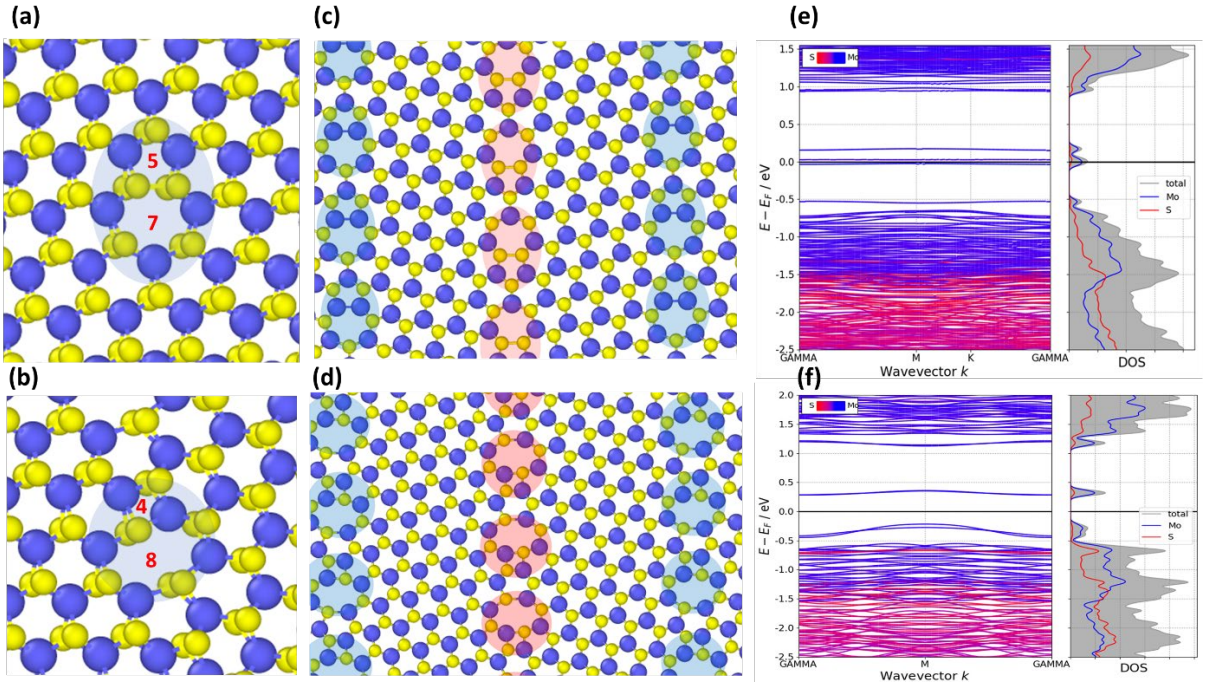

Figure 2: Free-standing MoS_2 monolayers with semiconducting GBs. *(a, b) Schematic representation of: (a) A polyhedral (5|7) edge dislocation highlighted by a shaded region and (b) a polyhedral (4|8)*

edge dislocation highlighted by a shaded region. (c, d) Formation of (c) (5|7) AC GBs and (d) (4|8) ZZ GBs by aligning parallel periodic arrays of equidistant dislocations with opposite orientations. Shaded regions represent edge dislocations, with red and blue colours signifying opposite orientations. The dislocation spacing is one hexagon, and the distance between the GBs is five hexagonal units. (e, f) Electronic band structure (left panel) and density of states (DOS, right panel) for MoS_2 with (e) (5|7) AC GBs and (f) (4|8) ZZ GBs. The partial DOS is calculated as an average over the d-orbitals of Mo atoms (blue) and the p-orbitals of S atoms (red). The total DOS is represented by the grey shaded region.

To satisfy periodic boundary conditions along all the directions, opposing GBs with distinct dislocation orientations were introduced. In (5|7) AC GBs, pentagons are at the top and heptagons at the bottom in one GB, and heptagons at the top and pentagons at the bottom in the opposite GB (Figure 2(c)). Similarly, for (4|8) ZZ GBs, quadrilles are at the top and octagons at the bottom in one GB, and octagons at the top and quadrilles at the bottom in the opposite GB (Figure 2(d)). To ensure negligible interactions between the GBs, we put them five hexagons apart (Figure 2(c) and 2(d)).

Both (5|7) and (4|8) GBs in freestanding MoS_2 monolayers show clear semiconducting behaviour in their electronic band structure (EBS, Figures 2(e, f) left panels). GB-induced states pin the Fermi level, evident in the localized peaks within the bandgap (Figures 2(e, f) right panels). PDOS reveals the GB-related peaks absent in pristine MoS_2, with Mo (blue) dominating over S (red) around the bandgap, suggesting Mo-centric defect states.

We further explored free-standing MoS_2 with conducting GBs. The (4|4P) mirror ZZ GB with four-fold-coordinated S-atoms (Figure 3(a)) and the Mo-Mo twin ZZ GB with five-fold-coordinated Mo-atoms (Figure 3(b)) were selected. The (4|4P) GB exhibits a 4-atom periodicity without additional shifts between the adjacent GBs along the GB axis (P direction). The five-hexagon separation was chosen to ensure negligible interactions between the GBs (Figure 3(c)). This setup allows us to isolate and study their unique metallic properties.

The metallic character of these GBs is evident from the dispersive bands intersecting Fermi level (FL) in their EBS (Figure 3(d) left panel). Contrary to the localized defect states observed in semiconducting GBs, the PDOS of these conducting GBs exhibits broad, primarily featureless peaks spanning the entire band gap (Figure 3(d) right panel). These characteristics are indicative of delocalized electronic states that facilitate metallic conduction along the GBs. Consequently, these GBs can be considered as one-dimensional metallic quantum wires embedded within the semiconducting MoS_2 monolayer.

The free-standing MoS_2 monolayers with GBs were placed on a six-layer Au(111) slab (Figure 4(a)). To maximize the binding energy, the epitaxial alignment between the bottom S-plane of the MoS_2 and the top surface layer of the gold substrate was optimized. This alignment was accomplished by rotating and shifting the MoS_2 monolayer to maximize the overlap of atoms across the interface. To eliminate lattice mismatch, a biaxial strain of $\leqslant$5% was applied to the gold substrate[11]. The atomic structures of the constructed samples were optimized using DFT calculations.

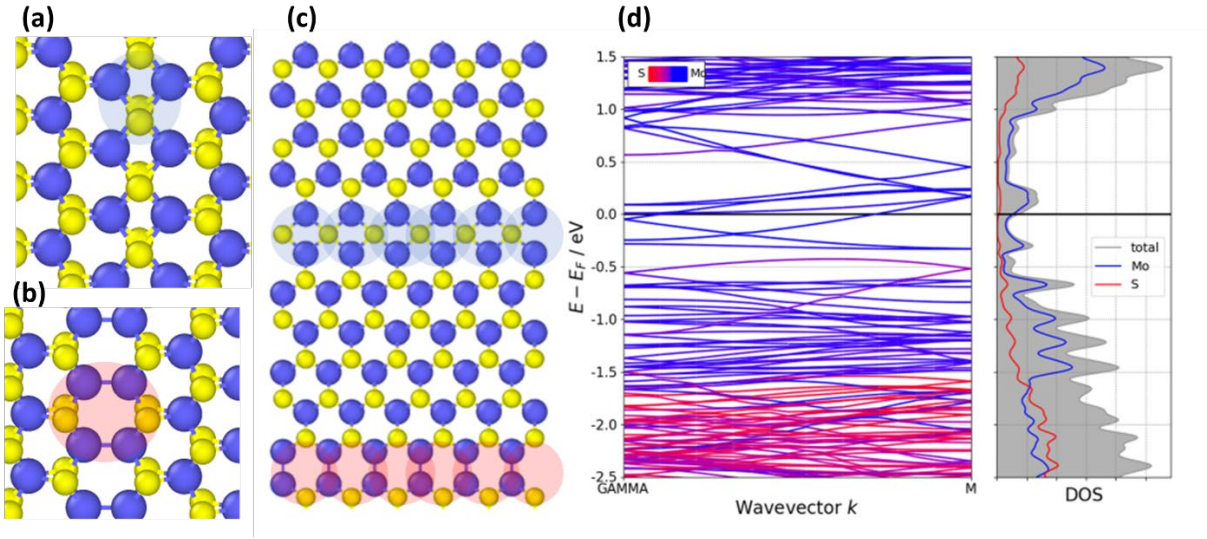

***Figure 3: Free-standing MoS_2 monolayers with conducting GBs**. (a, b) Schematic representation of polyhedral dislocations with (a) four-fold-coordinated S atoms highlighted by a shaded region and (b) five-fold-coordinated Mo atoms forming Mo-Mo bonds highlighted by a shaded region. (c) Mirror (4|4P) ZZ GB (blue shaded) and Mo-Mo ZZ GB (red shaded) formed by parallel periodic arrays of equi-distant dislocations. The distance between the GBs is five hexagonal units. (d) EBS (left panel) and DOS (right panel) for MoS_2 with mirror (4|4P) and Mo-Mo ZZ GBs. The PDOS is calculated as an average over the d-orbitals of Mo atoms (blue) and the p-orbitals of S atoms (red). The total DOS is represented by the grey shaded region.*

The key concept of our novel approach lies in exploring the spatial variations in the SBH at the MoS_2@Au heterojunction by employing atomically resolved PDOS calculations. Individual SBH values are extracted from atom-specific PDOS. The SBH is calculated as the difference between the CBM and the FL, which is defined as zero energy. Consequently, the SBH value directly corresponds to the CBM value.

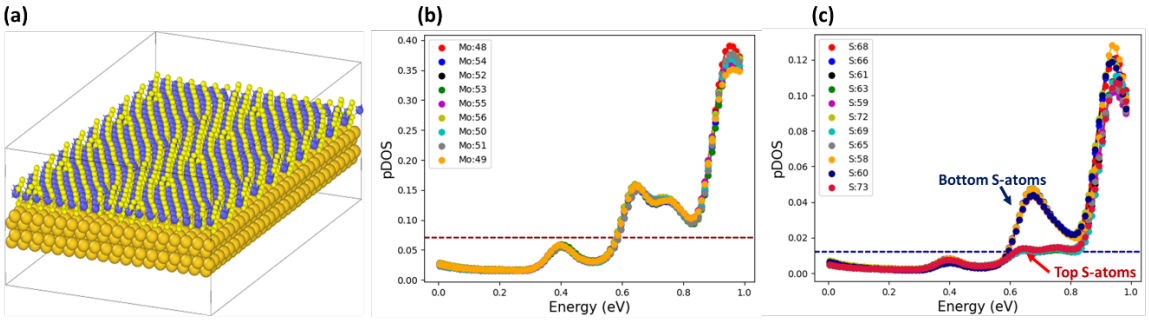

***Figure 4: PDOS analysis of gold-supported MoS_2 monolayer with GBs.** (a) Schematic illustration of the MoS_2@Au(111) sample with a six-layer gold substrate containing a MoS_2 monolayer with (5|7) GBs. Mo atoms are represented by blue spheres, S atoms are depicted by small yellow spheres, and larger yellow spheres represent Au atoms. (b, c) PDOS for randomly selected Mo atoms (b) and S atoms (c) in pristine MoS_2 on Au(111), indicated by atomic indexes and distinct colours. A noticeable difference in PDOS is observed between the top S atoms (located farther away from the gold substrate) and the bottom S atoms (located closer to the gold substrate). Dashed lines represent the effective zero value for PDOS of Mo and S atoms in the pristine MoS_2 on Au(111).*

Ideally, the pristine MoS_2 monolayer supported by Au should exhibit a step-like PDOS with an unoccupied bandgap and a well-defined CBM. However, as depicted in Figure 4(b, c), this idealized PDOS pattern is not observed. Instead, the bandgap shows a non-zero density of states and the CBM is broadened. This broadening is attributed to weak MoS_2-Au interactions and DFT smearing effects[56].

To obtain precise individual Schottky barrier height (SBH) values, the critical step involves accurately pinpointing the CBM – the energy level at which the PDOS transitions from zero to a non-zero value. In the specific case of MoS_2 on Au, identifying this transition necessitates establishing an effective zero, denoted as O_{eff}. The CBM, and consequently the SBH, are then determined as the energy level at which the PDOS exceeds this defined O_{eff}. It is worth noting that traditional SBH calculations typically yield an average SBH value across all MoS_2 atoms, a broad approximation that falls short of our specific requirements for individual SBH determination.

To set the O_{eff} for atom-specific PDOS, we use a pristine gold-supported MoS_2 monolayer as a reference (Figure 4(b, c)). The PDOS for each Mo atom (and S atom) in the pristine MoS_2 are identical. While the stronger Au-S interaction for the S atoms in the MoS_2 bottom sublayer causes a noticeable PDOS difference in the bottom sublayer as compared to the top one, this does not affect the setting of the effective zero (Figure 4(c)). Since the mean PDOS equals the atom-based PDOS for Mo (or S) atoms in pristine gold-supported MoS_2, the SBH value obtained via the EBS method can thus serve as the O_{eff} for atom-specific PDOS.

The SBH value of 0.67 eV for pristine MoS_2 on Au(111)[11] serves as a reference point in determining the atom-specific PDOS O_{eff} as shown by the dashed line in Figure 4(b, c). This reference point leads to O_{eff}=0.07 eV for Mo atoms and O_{eff}=0.007 eV for S atoms. The calculation of atomically resolved SBH values involves identifying the energy level at which the atom-specific PDOS surpasses its corresponding O_{eff} value, while ensuring that it remains greater than O_{eff} beyond this energy point. This method allows us to precisely determine SBH values for individual atoms within the MoS_2-Au heterojunction.

DFT calculations

Our DFT calculations employed the generalized Perdew-Burke-Ernzerhof[57] (GGA-PBE) functional and the projector-augmented wave (PAW) pseudopotential plane-wave method[58] as implemented in the Vienna ab initio simulation package (VASP)[59].

The PBE functional offers a good balance between accuracy and computational cost, making it suitable for our study, however, its limitations should be considered in the interpretation of results. No single functional is perfect; alternatives like LDA[60,61] or hybrid exchange-correlation potentials[62] might be better for specific properties or metals. While PBE has its limitations[63], it remains the most reliable choice for semiconductor-metal interface[44,49,64]. We note that more advanced methods exist for capturing the complex many-body effects of electron-electron interactions. One such method is the PBE+GW approximation[65], which goes beyond the PBE level. However, Zhong et al.[10] found that for weakly interacting MoS_2/Au, the difference between PBE and PBE+GW predictions is negligible.

We utilized $5d^{10}6s^1$ valence electrons for Au, $4p^6d^5s^1$ for Mo, and $3s^2p^4$ for S in the PAW pseudopotentials. Our DFT calculations employed a 6 × 6 × 1 Monkhorst–Pack k-point grid for geometry optimizations and a plane-wave basis set with a 520eV energy cut-off. The atomic samples were fully relaxed with residual force < 0.02 eV/Å per atom. Spin polarization and van der Waals corrections (Grimme's DFT-D2[59]) were used. Dipole corrections were applied along the normal to the Au(111)/MoS_2 heterojunction. Periodic boundary conditions were applied in all directions, with

vacuum layer of 20 Å along the normal to the interface (Figure 3(a)) to eliminate interactions between periodic images.

Results and discussion

In the following, we investigate the spatial variations in SBHs at MoS_2@Au heterojunctions and calculate the effective SBHs for MoS_2 monolayers with both conducting and semiconducting GBs. Our goal is to offer insights into the effects of defects on the electronic properties of Au/MoS_2 heterojunction and shedding light on the strategy for improving the design of metal-semiconductor heterojunction in general.

Spatial variations of SBH in Au-supported MoS_2 with semiconducting GBs

Figure 5(a) visually represents color-coded spatial variations in atom-resolved SBH for Au-supported MoS_2 with (5|7) GBs. In this case, the distance between neighbouring GBs is six hexagons, and the spacing between dislocations is one hexagon. In this illustration, red corresponds to the highest SBH values, while blue represents the lowest. Notably, the (5|7) AC GBs exhibit significantly lower SBH values in comparison to the grain interiors. Furthermore, the SBH values for atoms involved in forming Mo-Mo and S-S bonds within (5|7) edge dislocations tend to approach zero, as shown in Figure 5(a). To provide a comprehensive view of the SBH value distribution, Figure 5(c) displays a histogram. It is worth mentioning that the outliers in this histogram, characterized by the lowest SBH values, are primarily associated with atoms located at dislocation sites. Meanwhile, the majority of SBH values are concentrated around the values observed within the interior grain regions. Utilizing the atom-resolved SBH values, we calculated the effective SBH (*Eq. 7*) $\phi_{eff} = 0.5$ eV at room temperature for the MoS_2@Au heterojunction.

In contrast to the uniform SBH values within the grains, Figure 5(b) also reveals pronounced variations in SBH values at (4|8) ZZ GBs in Au-supported MoS_2. This observation aligns with previous studies that reported lower SBH values for edge dislocation atoms compared to grain interior atoms[66,67]. The SBH values are the lowest for atoms within the dislocation octagons (represented by blue atoms in Figure 5(b)). Conversely, the highest SBH values are observed for atoms within the quadrilaterals (represented by purple atoms in Figure 5(b)). Clearly, the SBH histogram for (4|8) ZZ GBs shows a resemblance to that of (5|7) AC GBs (Figure 5(d)), with the lowest SBH values associated with atoms at dislocations, and the majority of SBH values exhibiting a narrow distribution around 0.6 eV for atoms within the grain interior. Notably, a small fraction of GB atom contribute to even higher SBH values compared to the atoms within the grain interior. Employing the atom-resolved SBH values, we calculated the effective SBH (*Eq. 7*) $\phi_{eff} = 0.42$ eV at room temperature for MoS_2@Au heterojunction with the MoS_2 monolayer containing (4|8) ZZ GBs.

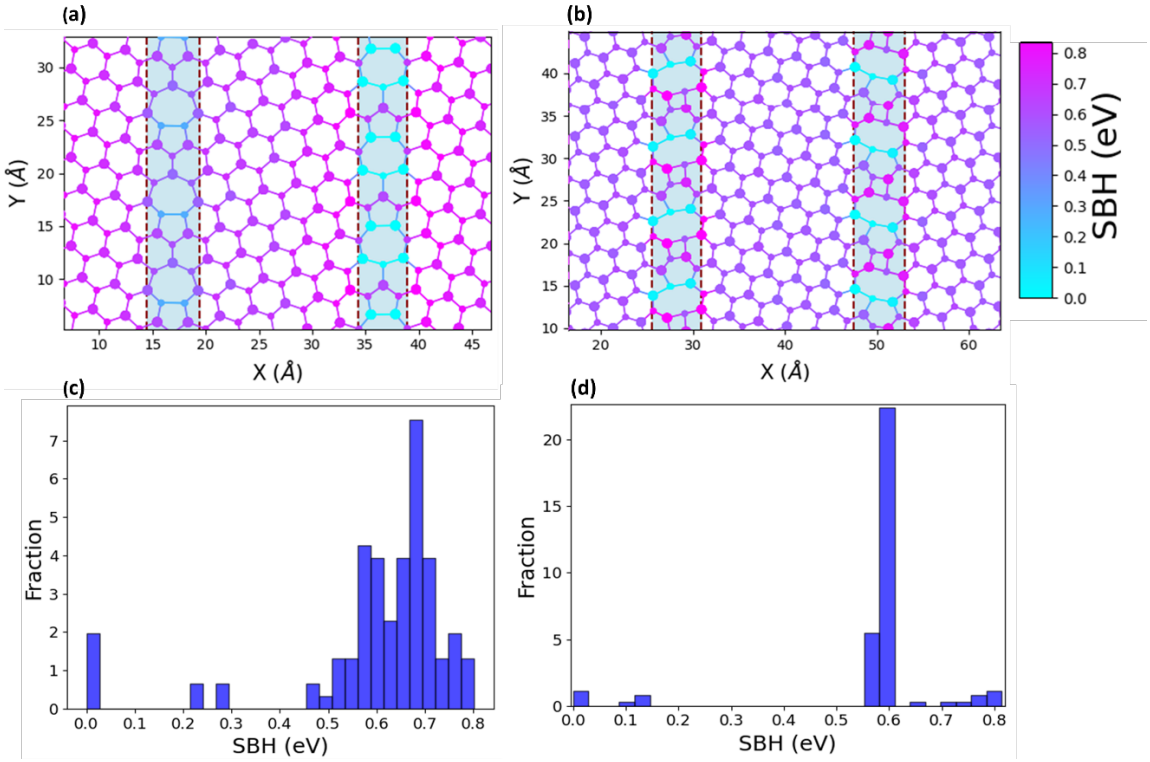

Figure 5: Spatial variations of SBH in Au-supported MoS_2 monolayer with semiconducting (5|7) AC (a) and (4|8) ZZ (b) GBs. *The color bar indicates the SBH value range. Shaded areas represent the GBs. Histogram of SBH values for MoS_2 monolayer with (5|7) AC (c) and with (4|8) ZZ (d) GBs. The distance between neighboring GBs is six hexagons, and the spacing between dislocations is one hexagon.*

Spatial variations of SBH in Au-supported MoS_2 with conducting mirror GBs

We employed our approach to investigate an Au-supported MoS_2 monolayer with conducting (4|4P) and Mo-Mo ZZ GBs. Spatial variations in atom-resolved SBH are visualized in Figure 6(a) through colour coding, wherein red denotes the highest SBH values while blue indicates the lowest. Notably, the GBs exhibit the lowest SBH values, effectively acting as one-dimensional metallic wires embedded within the semiconducting MoS_2 monolayer, as demonstrated in Figure 6(a). The SBH values within the grain interior indicate a semiconducting domain. The histogram presented in Figure 6(b) reveals a bimodal distribution of SBH values. The first peak corresponds to the lowest values, approaching zero, associated with both the conducting (4|4P) and Mo-Mo ZZ GBs. In contrast, the second peak encompasses the higher SBH values characteristic of the semiconducting grain interior. This bimodal distribution provides compelling evidence for the distinct electronic character of the GBs and the semiconducting region of the MoS_2 monolayer. Using the atom-resolved values, ϕ_i, we calculated the effective SBH (*Eq. 7*) $\phi_{eff} = 0.23$ eV at room temperature for MoS_2@Au heterojunction with conducting GBs.

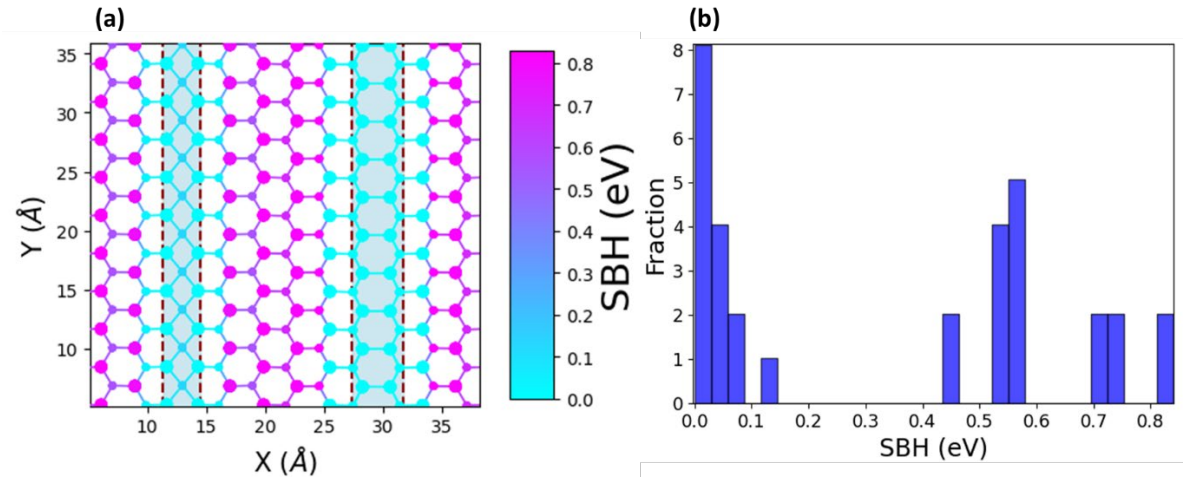

Figure 6: Spatial variations of SBH in an Au-supported MoS_2 monolayer containing two types of GBs: conducting (4\|4P) and Mo-Mo ZZ GBs. *(a) The GBs are formed by parallel periodic arrays of equi-distant dislocations. The color bar on the left indicates the SBH value range. Shaded areas represent the GBs. (b) Histogram of SBH values for the MoS_2 monolayer with (4\|4P) ZZ and Mo-Mo ZZ GBs. The distance between neighboring GBs is five hexagons, and the dislocations are packed in a head-to-tail fashion.*

Discussion

Recent years have seen a growing body of experimental SBH measurements for MoS_2@Au heterojunctions reported in the literature. For example, Bampoulis et al.[47] reported an experimentally measured SBH of 0.53 eV for MoS_2@Au, which falls below the range predicted by DFT calculations (0.65 eV - 0.8 eV)[8,9,11,15,25]. Similarly McDonnell et al. [68] confirmed that intrinsic defects in MoS_2 dominate the metal@MoS_2 contact resistance and provide a low SBH. Perini et al.[69] observed a significantly lower SBH of 0.44 eV for MoS_2@Au junctions. They attributed this reduction to strong FL pinning at the interface caused by the presence of numerous defects in MoS_2. Several experimental studies report SBH values for MoS_2@Au junctions that deviate from those predicted by DFT calculations. Kim et al.[15] measured an SBH of 0.33 eV, attributing the discrepancy to stronger FL pinning and the influence of defects. This trend of lower experimental values compared to DFT predictions continues, with Kaushik et al.[70] reporting an even lower SBH of 0.13 eV. In contrast, Liu et al.[71] achieved a remarkably low SBH of 0.06 eV using exceptionally clean and atomically flat interfaces, minimizing the impact of defects and FL pinning.

Thus, the experimental measurements of SBH in MoS_2@Au junctions reveal significant variations within and between samples. Crucially, a persistent discrepancy exists between these experimental SBH values and those predicted by DFT calculations. This gap likely stems from a combined effect of phenomena not fully captured by DFT, such as the presence of defects, which are typically neglected in DFT calculations, and limitations of the band alignment method based on Schottky-Mott rule[20] in accurately predicting SBH.

Conventional methods assume a uniform SBH across the interface, leading to inconsistencies with experimental data. Our novel, atom-based approach captures the spatial variations of SBH within MoS_2 layers, overcoming this limitation and represents a significant improvement over conventional DFT models and exhibits closer alignment with experimental measurements. By explicitly accounting for the inherent inhomogeneities like defects and impurities, we move beyond the simplified Schottky-

Mott rule[20]. This approach yields more realistic effective SBH values (0.2-0.5eV) in MoS_2@Au junctions, for MoS_2 with conducting GBs, which is closer to experimental measurements. Our results, which closely match experimental observations, highlight the crucial role of spatial variations, especially in defect-rich MoS_2. This emphasizes the importance of moving beyond single-point characterization and embracing a spatially-aware understanding of SBH, particularly in defect-rich MoS_2 layers. For example, our findings indicate that a MoS_2 monolayer with a high density of conducting defects can result in a significantly reduced SBH. Hence, the present work underscores the importance of controlling defect character and density so as to precisely regulate the SBH values. While we present the novel approach in the context of MoS_2@Au heterojunction, its reliance on readily obtainable electronic structure information makes it potentially applicable to a wide range of metal-semiconductor heterojunctions. Although our current work focuses on GBs, the novel PDOS-based atom-specific analysis is applicable to other defect types such as vacancies and anti-site defects in MoS2 monolayer. Accurately incorporating all defect types and their distributions into the model for a perfect match with experimental data presents a significant challenge. However, our primary goal here is not to achieve quantitative agreement with specific experiments, but rather to propose a model that provides a deeper understanding of the underlying mechanism at play. While a complete defect characterization is ideal, this model offers valuable insights into the crucial roles of defect types and density in determining the SBH values.

Beyond point and extended defects, Wu et al.[72] highlight potential formation of local amorphous structures during metal contact fabrication on MoS_2. These structures can introduce interfacial disorder and variations in SBH due to their complex impact on morphology, electronic structure, and charge transport. Our versatile approach can readily model this effect by incorporating an amorphous layer with relevant properties. Furthermore, the strength of our atom-level PDOS analysis lies in its scalability. This allows for seamless extension of our approach to study MoS_2@Au heterojunctions incorporating multilayer MoS_2 configurations.

While our approach offers valuable insights into SBH variations, it is essential to acknowledge its limitations. First, atomic PDOS may not accurately capture interfacial phenomena[16,19,73], potentially affecting the overall accuracy of SBH calculations. Integrating our approach with other theoretical frameworks or experimental techniques could provide a more comprehensive understanding of SBH variations and incorporating machine learning approaches might improve SBH predictions[74].

Second, a significant limitation of the atomistic approach is its computational complexity, particularly for polycrystalline MoS_2 monolayers with extensive defects. Balancing accuracy and computational feasibility may require compromises in the level of detail of SBH calculations.

Third, our current model focuses on intrinsic properties of MoS_2 monolayers and their impact on the SBH at MoS_2/Au interfaces. However, a crucial aspect for practical applications is the potential influence of extrinsic factors that can cause inhomogeneity in the MoS_2 layer. These factors include substrates, photoresist residues, and tapes used during device fabrication[15,64,75]. Undoubtedly, such inhomogeneities can introduce variations in the material properties of MoS_2@Au heterojunctions. In real-world devices, these variations might become more significant than the effects explored in this work, potentially overshadowing the intrinsic factors we have addressed. An interesting future work is to incorporate these inhomogeneity effects.

Finally, our model is specifically designed for vertical MoS_2@Au contact structures similar to those proposed by Murali et al.[76] In these structures, the current flows vertically through the MoS_2 monolayer, and the current density is expected to be almost uniform underneath the contact area. We recognize this limitation in our model, which assumes a quasi-uniform current density across the

contact area. Another interesting future work could involve extending the model to incorporate the effects of current crowding in lateral field-effect transistor (FET) structures[76].

It is important to highlight that direct atomic-resolution measurements of SBH remain a challenging task. Techniques such as STM offer limited precision[38] and achieving accurate SBH determination requires knowledge of every interfacial atom, which can be hindered by factors like surface roughness and atomic diffusion during the measurements. Our present approach offers critical insights into the non-uniform SBH distributions at MoS_2/metal interfaces and presents an alternative avenue to predict the atomic SBH if the atomic structure of the interface is known.

Conclusions

Our newly proposed atomic-scale approach for SBH calculations offers detailed insights into the local electronic properties at MoS_2@metal heterojunctions, providing more accurate SBH predictions than traditional methods. It leverages atomically resolved SBHs and considers the atomic arrangement of defects in MoS_2 monolayers, addressing the limitations of traditional DFT approaches that average over atoms and tend to overestimate experimental SBH measurements. This new approach yields results identical to conventional DFT methods for perfect MoS_2, ensuring consistency and generalizability. Moreover, it significantly improves the agreement between experimental findings and theoretical predictions for Au-supported defective MoS_2 monolayers, highlighting its improved accuracy and predictive power. Validation through its application to MoS_2@Au heterojunctions containing both conducting and semiconducting grain boundaries, reveals an inhomogeneous distribution of SBH values attributed to defects. Lower or even zero SBH values are observed at grain boundaries and dislocation cores. We further show that the variation of local SBH is able to modulate the overall effective SBH, and results in better agreement with experimental data, confirming the accuracy and predictive power of our approach while providing insights into the wide variations observed in experimentally measured SBH values. This atomistic approach predicts non-uniform SBH variations at MoS_2@metal heterojunctions, resolving SBHs at the individual atomic level and offering valuable insights into defect-induced inhomogeneities critical for accurate heterojunction modelling. It is expected that its relevance and feasibility extend beyond Au/MoS_2 heterojunctions, encompassing a wide range of metal-semiconductor heterojunctions, and are expected to grow with the rapid advancements in nanoelectronics.

Acknowledgements

This work was supported by the National Research Foundation, Singapore under Award No. NRF-CRP24-2020-0002. Zhang Y.W. acknowledges the support from Singapore A*STAR SERC CRF Award. The use of computing resources at the A*STAR Computational Centre and National Supercomputer Centre, Singapore is gratefully acknowledged.

Citations

(1) Zhou, H.; Loi, S.; Ang, K. W.; Zhang, Y. W. Recent Advances in In-Memory Computing: Exploring Memristor and Memtransistor Arrays with 2D Materials. *Nano-Micro Lett.* **2024**, *16*, 121. https://doi.org/ttps://link.springer.com/article/10.1007/s40820-024-01335-2.

(2) Zhang, C.; Zhou, H.; Chen, S.; Zhang, G.; Yu, Z. G.; Chi, D.; Zhang, Y. W.; Ang, K. W. Recent Progress on 2D Materials-Based Artificial Synapses. *Crit. Rev. Solid State Mater. Sci.* **2021**, 1935212. https://doi.org/10.1080/10408436.2021.1935212.

(3) Tung, R. The Physics and Chemistry of the Schottky Barrier Height. *Appl. Phys. Rev.* **2014**, *1* (1), 011304. https://doi.org/10.1063/1.4858400.

(4) Pollmann, E.; Sleziona, S.; Foller, T.; Hagemann, U.; Gorynski, C.; Petri, O.; Madauß, L.; Breuer, L.; Schleberger, M. Large-Area, Two-Dimensional MoS2 Exfoliated on Gold: Direct Experimental Access to the Metal-Semiconductor Interface. *ACS Omega* **2021**, *6* (24), 15929–15939. https://doi.org/10.1021/acsomega.1c01570.

(5) Radisavljevic, B.; Radenovic, A.; Brivio, J.; Giacometti, V.; Kis, A. Single-Layer MoS2 Transistors. *Nat. Nanotechhology* **2011**, *6*, 147–150. https://doi.org/10.1038/nnano.2010.279.

(6) Chen, J. R.; Odenthal, P. M.; Swartz, A. G.; Floyd, G. C.; Wen, H.; Luo, K. Y.; Kawakami, R. K. Control of Schottky Barriers in Single Layer MoS2 Transistors with Ferromagnetic Contacts. *Nano Lett.* **2013**, *13* (7), 3106–3110. https://doi.org/10.1021/nl4010157.

(7) Liu, H.; Si, M.; Deng, Y.; Neal, A. T.; Du, Y.; Najmaei, S.; Ajayan, P. M.; Lou, J.; Ye, P. D. Switching Mechanism in Single-Layer Molybdenum Disulfide Transistors: An Insight into Current Flow across Schottky Barriers. *ACS Nano* **2014**, *8* (1), 1031–1038. https://doi.org/10.1021/nn405916t.

(8) Pan, Y.; Gu, J.; Tang, H.; Zhang, X.; Li, J.; Shi, B.; Yang, J.; Zhang, H.; Yan, J.; Liu, S.; Hu, H.; Wu, M.; Lu, J. Reexamination of the Schottky Barrier Heights in Monolayer MoS2 Field-Effect Transistors. *ACS Appl. Nano Mater.* **2019**, *2* (8), 4717–4726. https://doi.org/10.1021/acsanm.9b00200.

(9) Kim, G. S.; Kim, S. H.; Park, J.; Han, K. H.; Kim, J.; Yu, H. Y. Schottky Barrier Height Engineering for Electrical Contacts of Multilayered MoS2 Transistors with Reduction of Metal-Induced Gap States. *ACS Nano* **2018**, *12* (6), 6292–6300. https://doi.org/10.1021/acsnano.8b03331.

(10) Zhong, H.; Quhe, R.; Wang, Y.; Ni, Z.; Ye, M.; Song, Z.; Pan, Y.; Yang, J.; Yang, L.; Lei, M.; Shi, J.; Lu, J. Interfacial Properties of Monolayer and Bilayer MoS 2 Contacts with Metals: Beyond the Energy Band Calculations. *Sci. Rep.* **2016**, *6* (March), 21786. https://doi.org/10.1038/srep21786.

(11) Sorkin, V.; Zhou, H.; Yu, Z. G.; Ang, K. W.; Zhang, Y. W. The Effects of Point Defect Type, Location, and Density on the Schottky Barrier Height of Au/MoS2 Heterojunction: A First-Principles Study. *Sci. Rep.* **2022**, *12* (1), 18001–18015. https://doi.org/10.1038/s41598-022-22913-7.

(12) Kang, J.; Liu, W.; Sarkar, D.; Jena, D.; Banerjee, K. Computational Study of Metal Contacts to Monolayer Transition-Metal Dichalcogenide Semiconductors. *Phys. Rev. X* **2014**, *4* (3), 031005. https://doi.org/10.1103/PhysRevX.4.031005.

(13) An, J.; Voelkl, E.; Suk, J.; Li, X.; Magnuson, C. W.; Fu, L.; Tiemeijer, P.; Bischoff, M.; Freitag, B.; Popova, E.; Ruoff, R. S. Domain (Grain) Boundaries and Evidence of " Twin-Like " Structures in CVD Grown Graphene. *ACS Nano* **2011**, *5* (4), 2433–2439. https://doi.org/https://pubs.acs.org/doi/10.1021/nn103102a.

(14) Popov, I.; Seifert, G.; Tománek, D. Designing Electrical Contacts to MoS 2 Monolayers: A Computational Study. *Phys. Rev. Lett.* **2012**, *108* (15), 156802. https://doi.org/10.1103/PhysRevLett.108.156802.

(15) Kim, C.; Moon, I.; Lee, D.; Choi, M. S.; Ahmed, F.; Nam, S.; Cho, Y.; Shin, H. J.; Park, S.; Yoo, W. J. Fermi Level Pinning at Electrical Metal Contacts of Monolayer Molybdenum Dichalcogenides. *ACS Nano* **2017**, *11* (2), 1588–1596.

https://doi.org/10.1021/acsnano.6b07159.

(16) Gong, C.; Colombo, L.; Wallace, R. M.; Cho, K. The Unusual Mechanism of Partial Fermi Level Pinning at Metal-MoS 2 Interfaces. *Nano Lett.* **2014**, *14* (4), 1714–1720. https://doi.org/10.1021/nl403465v.

(17) Feng, L. P.; Su, J.; Li, D. P.; Liu, Z. T. Tuning the Electronic Properties of Ti-MoS2 Contacts through Introducing Vacancies in Monolayer MoS2. *Phys. Chem. Chem. Phys.* **2015**, *17* (10), 6700–6704. https://doi.org/10.1039/c5cp00008d.

(18) Chen, W.; Santos, E. J. G.; Zhu, W.; Kaxiras, E.; Zhang, Z. Tuning the Electronic and Chemical Properties of Monolayer MoS2 Adsorbed on Transition Metal Substrates. *Nano Lett.* **2013**, *13* (2), 509–514. https://doi.org/© 2013 American Chemical Society 509 dx.doi.org/10.1021/nl303909f |.

(19) Li, M.; Lan, F.; Yang, W.; Ji, Z.; Zhang, Y.; Xi, N.; Xin, X.; Jin, X.; Li, G. Influence of MoS2-Metal Interface on Charge Injection: A Comparison between Various Metal Contacts. *Nanotechnology* **2020**, *31* (39), 395713. https://doi.org/10.1088/1361-6528/ab9cf6.

(20) Park, S.; Schultz, T.; Shin, D.; Mutz, N.; Aljarb, A.; Kang, H. S.; Lee, C. H.; Li, L. J.; Xu, X.; Tung, V.; List-Kratochvil, E. J. W.; Blumstengel, S.; Amsalem, P.; Koch, N. The Schottky-Mott Rule Expanded for Two-Dimensional Semiconductors: Influence of Substrate Dielectric Screening. *ACS Nano* **2021**, *15* (9), 14794–14803. https://doi.org/10.1021/acsnano.1c04825.

(21) Su, J.; Feng, L.; Zhang, Y.; Liu, Z. The Modulation of Schottky Barriers of Metal-MoS2 Contacts: Via BN-MoS2 Heterostructures. *Phys. Chem. Chem. Phys.* **2016**, *18* (25), 16882–16889. https://doi.org/10.1039/c6cp02132h.

(22) Voiry, D.; Fullon, R.; Yang, J.; De Carvalho Castro E Silva, C.; Kappera, R.; Bozkurt, I.; Kaplan, D.; Lagos, M. J.; Batson, P. E.; Gupta, G.; Mohite, A. D.; Dong, L.; Er, D.; Shenoy, V. B.; Asefa, T.; Chhowalla, M. The Role of Electronic Coupling between Substrate and 2D MoS2 Nanosheets in Electrocatalytic Production of Hydrogen. *Nat. Mater.* **2016**, *15* (9), 1003–1009. https://doi.org/10.1038/nmat4660.

(23) Yang, M.; Kim, T. Y.; Lee, T.; Hong, S. Nanoscale Enhancement of Photoconductivity by Localized Charge Traps in the Grain Structures of Monolayer MoS2. *Sci. Rep.* **2018**, *8* (1), 15822. https://doi.org/10.1038/s41598-018-34209-w.

(24) Yu, H.; Gupta, S.; Kutana, A.; Yakobson, B. I. Dimensionality-Reduced Fermi Level Pinning in Coplanar 2D Heterojunctions. *J. Phys. Chem. Lett.* **2021**, *12* (17), 4299–4305. https://doi.org/10.1021/acs.jpclett.0c03663.

(25) Somvanshi, D.; Kallatt, S.; Venkatesh, C.; Nair, S.; Gupta, G.; Anthony, J. K.; Karmakar, D.; Majumdar, K. Nature of Carrier Injection in Metal/2D-Semiconductor Interface and Its Implications for the Limits of Contact Resistance. *Phys. Rev. B* **2017**, *96* (20), 205423. https://doi.org/10.1103/PhysRevB.96.205423.

(26) Yazyev, O. V.; Kis, A. MoS2 and Semiconductors in the Flatland. *Mater. Today* **2015**, *18* (1), 20–30. https://doi.org/10.1016/j.mattod.2014.07.005.

(27) Sorkin, V.; Pan, H.; Shi, H.; Quek, S. Y. Y.; Zhang, Y. W. Nanoscale Transition Metal Dichalcogenides: Structures, Properties, and Applications. *Crit. Rev. Solid State Mater. Sci.* **2014**, *39* (5), 319–367. https://doi.org/10.1080/10408436.2013.863176.

(28) Tumino, F.; Casari, C. S.; Li Bassi, A.; Tosoni, S. Nature of Point Defects in Single-Layer MoS2Supported on Au(111). *J. Phys. Chem. C* **2020**, *124* (23), 12424–12431. https://doi.org/10.1021/acs.jpcc.0c01477.

(29) Yang, J.; Bussolotti, F.; Kawai, H.; Goh, K. E. J. Tuning the Conductivity Type in Monolayer WS2 and MoS2 by Sulfur Vacancies. *Phys. Status Solidi - Rapid Res. Lett.* **2020**, *14* (9), 2000248. https://doi.org/10.1002/pssr.202000248.

(30) Liu, D.; Guo, Y.; Fang, L.; Robertson, J. Sulfur Vacancies in Monolayer MoS2 and Its Electrical Contacts. *Appl. Phys. Lett.* **2013**, *103* (18), 183113. https://doi.org/10.1063/1.4824893.

(31) Komsa, H. P.; Krasheninnikov, A. V. Native Defects in Bulk and Monolayer MoS2 from First Principles. *Phys. Rev. B* **2015**, *91* (12), 125304. https://doi.org/10.1103/PhysRevB.91.125304.

(32) Wang, L.; Liao, W.; Wong, S. L.; Yu, Z. G.; Li, S.; Lim, Y. F.; Feng, X.; Tan, W. C.; Huang, X.; Chen, L.; Liu, L.; Chen, J.; Gong, X.; Zhu, C.; Liu, X.; Zhang, Y. W.; Chi, D.; Ang, K. W. Artificial Synapses Based on Multiterminal Memtransistors for Neuromorphic Application. *Adv. Funct. Mater.* **2019**, *29* (25), 1901106. https://doi.org/10.1002/adfm.201901106.

(33) Li, D.; Wu, B.; Zhu, X.; Wang, J.; Ryu, B.; Lu, W. D.; Lu, W.; Liang, X. MoS2 Memristors Exhibiting Variable Switching Characteristics toward Biorealistic Synaptic Emulation. *ACS Nano* **2018**, *12* (9), 9240–9252. https://doi.org/10.1021/acsnano.8b03977.

(34) Jin, H.; Guo, C.; Liu, X.; Liu, J.; Vasileff, A.; Jiao, Y.; Zheng, Y.; Qiao, S. Z. Emerging Two-Dimensional Nanomaterials for Electrocatalysis. *Chem. Rev.* **2018**, *118* (13), 6337–6408. https://doi.org/10.1021/acs.chemrev.7b00689.

(35) Upadhyay, S. N.; Satrughna, J. A. K.; Pakhira, S. Recent Advancements of Two-Dimensional Transition Metal Dichalcogenides and Their Applications in Electrocatalysis and Energy Storage. *Emergent Mater.* **2021**, *4* (4), 951–970. https://doi.org/10.1007/s42247-021-00241-2.

(36) Zhou, H.; Sorkin, V.; Chen, S.; Yu, Z. G.; Ang, K. W.; Zhang, Y. W. Design-Dependent Switching Mechanisms of Schottky-Barrier-Modulated Memristors Based on 2D Semiconductor. *Adv. Electron. Mater.* **2023**, *9* (6), 2201252. https://doi.org/10.1002/aelm.202201252.

(37) Cheng, P.; Sun, K.; Hu, Y. H. Memristive Behavior and Ideal Memristor of 1T Phase MoS2 Nanosheets. *Nano Lett.* **2016**, *16* (1), 572–576. https://doi.org/10.1021/acs.nanolett.5b04260.

(38) Sangwan, V. K.; Hersam, M. C. Electronic Transport in Two-Dimensional Materials. *Annu. Rev. Phys. Chem.* **2018**, *69* (1), 299–325. https://doi.org/10.1146/annurev-physchem-050317-021353.

(39) Wang, J.; Ma, F.; Sun, M. Graphene, Hexagonal Boron Nitride, and Their Heterostructures: Properties and Applications. *RSC Adv.* **2017**, *7* (27), 16801–16822. https://doi.org/10.1039/C7RA00260B.

(40) Bhimanapati, G. R.; Lin, Z.; Meunier, V.; Jung, Y.; Cha, J.; Das, S.; Xiao, D.; Son, Y.; Strano, M. S.; Cooper, V. R.; Liang, L.; Louie, S. G.; Ringe, E.; Zhou, W.; Kim, S. S.; Naik, R. R.; Sumpter, B. G.; Terrones, H.; Xia, F.; Wang, Y.; Zhu, J.; Akinwande, D.; Alem, N.; Schuller, J. A.; Schaak, R. E.; Terrones, M.; Robinson, J. A. Recent Advances in Two-Dimensional Materials beyond Graphene. *ACS Nano* **2015**, *9* (12), 11509–11539. https://doi.org/10.1021/acsnano.5b05556.

(41) Akhtar, M.; Anderson, G.; Zhao, R.; Alruqi, A.; Mroczkowska, J. E.; Sumanasekera, G.; Jasinski, J. B. Recent Advances in Synthesis, Properties, and Applications of Phosphorene. *npj 2D Mater. Appl.* **2017**, *1* (1), 5. https://doi.org/10.1038/s41699-017-0007-5.

(42) Balendhran, S.; Walia, S.; Nili, H.; Sriram, S.; Bhaskaran, M. Elemental Analogues of Graphene: Silicene, Germanene, Stanene, and Phosphorene. *Small* **2015**, *11* (6), 640–652. https://doi.org/10.1002/smll.201402041.

(43) Wang, H.; Yuan, H.; Sae Hong, S.; Li, Y.; Cui, Y. Physical and Chemical Tuning of Two-Dimensional Transition Metal Dichalcogenides. *Chem. Soc. Rev.* **2015**, *44* (9), 2664–2680. https://doi.org/10.1039/C4CS00287C.

(44) Tung, R. T. Formation of an Electric Dipole at Metal-Semiconductor Interfaces. *Phys. Rev. B* **2001**, *64* (20), 295310. https://doi.org/10.1103/PhysRevB.64.205310.

(45) Sotthewes, K.; Van Bremen, R.; Dollekamp, E.; Boulogne, T.; Nowakowski, K.; Kas, D.; Zandvliet, H. J. W.; Bampoulis, P. Universal Fermi-Level Pinning in Transition-Metal Dichalcogenides. *J. Phys. Chem. C* **2019**, *123* (9), 5411–5420. https://doi.org/10.1021/acs.jpcc.8b10971.

(46) Farmanbar, M.; Brocks, G. First-Principles Study of van Der Waals Interactions and Lattice Mismatch at MoS2/Metal Interfaces. *Phys. Rev. B* **2016**, *93* (8), 085304. https://doi.org/10.1103/PhysRevB.93.085304.

(47) Bampoulis, P.; Van Bremen, R.; Yao, Q.; Poelsema, B.; Zandvliet, H. J. W.; Sotthewes, K. Defect Dominated Charge Transport and Fermi Level Pinning in MoS2/Metal Contacts. *ACS Appl. Mater. Interfaces* **2017**, *9* (22), 19278–19286. https://doi.org/10.1021/acsami.7b02739.

(48) Sangwan, V. K.; Lee, H. S.; Bergeron, H.; Balla, I.; Beck, M. E.; Chen, K. S.; Hersam, M. C. Multi-Terminal Memtransistors from Polycrystalline Monolayer Molybdenum Disulfide. *Nature* **2018**, *554* (7693), 500–504. https://doi.org/10.1038/nature25747.

(49) Moon, B. H.; Han, G. H.; Kim, H.; Choi, H.; Bae, J. J.; Kim, J.; Jin, Y.; Jeong, H. Y.; Joo, M. K.; Lee, Y. H.; Lim, S. C. Junction-Structure-Dependent Schottky Barrier Inhomogeneity and Device Ideality of Monolayer MoS2 Field-Effect Transistors. *ACS Appl. Mater. Interfaces* **2017**, *9* (12), 11240–11246. https://doi.org/10.1021/acsami.6b16692.

(50) Ye, Z.; Tan, C.; Huang, X.; Ouyang, Y.; Yang, L.; Wang, Z.; Dong, M. Emerging MoS2 Wafer-Scale Technique for Integrated Circuits. *Nano-Micro Letters*. 2023, p 38. https://doi.org/10.1007/s40820-022-01010-4.

(51) Lang, P. F. Fermi Energy, Metals and the Drift Velocity of Electrons. *Chem. Phys. Lett.* **2021**, *770*, 138447. https://doi.org/10.1016/j.cplett.2021.138447.

(52) Zhou, W.; Zou, X.; Najmaei, S.; Liu, Z.; Shi, Y.; Kong, J.; Lou, J.; Ajayan, P. M.; Yakobson, B. I.; Idrobo, J. C. Intrinsic Structural Defects in Monolayer Molybdenum Disulfide. *Nano Lett.* **2013**, *13* (6), 2615–2622. https://doi.org/10.1021/nl4007479.

(53) Wong, C. P. Y.; Troadec, C.; Wee, A. T. S.; Goh, K. E. J. Gaussian Thermionic Emission Model for Analysis of Au/Mo S2 Schottky-Barrier Devices. *Phys. Rev. Appl.* **2020**, *14* (5), 054027. https://doi.org/10.1103/PhysRevApplied.14.054027.

(54) Zou, X.; Yakobson, B. I. An Open Canvas - 2D Materials with Defects, Disorder, and Functionality. *Acc. Chem. Res.* **2015**, *48* (1), 73–80. https://doi.org/10.1021/ar500302q.

(55) Liu, Y.; Zou, X.; Yakobson, B. I. Dislocations and Grain Boundaries in Two-Dimensional Boron Nitride. *ACS Nano* **2012**, *6* (8), 7053–7058. https://doi.org/10.1021/nn302099q.

(56) Moses, P. G.; Miao, M.; Yan, Q.; Van De Walle, C. G. Hybrid Functional Investigations of Band Gaps and Band Alignments for AlN, GaN, InN, and InGaN. *J. Chem. Phys.* **2011**, *134* (8), 084703. https://doi.org/10.1063/1.3548872.

(57) Perdew, J. P.; Burke, K.; Ernzerhof, M. Generalized Gradient Approximation Made Simple. *Phys. Rev. Lett.* **1996**, *77* (18), 3865–3868. https://doi.org/10.1103/PhysRevLett.77.3865.

(58) Blöchl, P. E. Projector Augmented-Wave Method. *Phys. Rev. B* **1994**, *50* (24), 17953–17979.

https://doi.org/10.1103/PhysRevB.50.17953.

(59) Kresse, G.; Furthmüller, J. Efficient Iterative Schemes for Ab Initio Total-Energy Calculations Using a Plane-Wave Basis Set. *Phys. Rev. B* **1996**, *54* (16), 11169–11186. https://doi.org/10.1103/PhysRevB.54.11169.

(60) Ravindran, P.; Fast, L.; Korzhavyi, P. A.; Johansson, B.; Wills, J.; Eriksson, O. Density Functional Theory for Calculation of Elastic Properties of Orthorhombic Crystals: Application to TiSi2. *J. Appl. Phys.* **1998**, *84* (9), 4891–4904. https://doi.org/10.1063/1.368733.

(61) Petukhov, A. G.; Mazin, I. I.; Chioncel, L.; Lichtenstein, A. I. Correlated Metals and the LDA+U Method. *Phys. Rev. B* **2003**, *67* (15), 153106. https://doi.org/10.1103/PhysRevB.67.153106.

(62) Råsander, M.; Moram, M. A. On the Accuracy of Commonly Used Density Functional Approximations in Determining the Elastic Constants of Insulators and Semiconductors. *J. Chem. Phys.* **2015**, *143* (14), 144104. https://doi.org/10.1063/1.4932334.

(63) Perdew, J.; Burke, K.; Ernzerhof, M. PBE and PBE0. *Phys. Rev. Lett.* **1996**, *77* (18), 3865–3868. https://doi.org/10.1103/PhysRevLett.77.3865.

(64) Fang, Q.; Zhao, X.; Xia, C.; Ma, F. Interfacial Defect Engineering on Electronic States and Electrical Properties of MoS2/Metal Contacts. *J. Alloys Compd.* **2021**, *864*, 158134. https://doi.org/10.1016/j.jallcom.2020.158134.

(65) Caruso, F.; Rohr, D. R.; Hellgren, M.; Ren, X.; Rinke, P.; Rubio, A.; Scheffler, M. Bond Breaking and Bond Formation: How Electron Correlation Is Captured in Many-Body Perturbation Theory and Density-Functional Theory. *Phys. Rev. Lett.* **2013**, *110* (14), 1–5. https://doi.org/10.1103/PhysRevLett.110.146403.

(66) Najmaei, S.; Yuan, J.; Zhang, J.; Ajayan, P.; Lou, J. Synthesis and Defect Investigation of Two-Dimensional Molybdenum Disulfide Atomic Layers. *Acc. Chem. Res.* **2015**, *48* (1), 31–40. https://doi.org/10.1021/ar500291j.

(67) Man, P.; Srolovitz, D.; Zhao, J.; Ly, T. H. Functional Grain Boundaries in Two-Dimensional Transition-Metal Dichalcogenides. *Acc. Chem. Res.* **2021**, *54* (22), 4191–4202. https://doi.org/10.1021/acs.accounts.1c00519.

(68) McDonnell, S.; Addou, R.; Buie, C.; Wallace, R. M.; Hinkle, C. L. Defect-Dominated Doping and Contact Resistance in MoS2. *ACS Nano* **2014**, *8* (3), 2880–2888. https://doi.org/10.1021/nn500044q.

(69) Perini, C. J.; Basnet, P.; West, M. P.; Vogel, E. M. Impact of Synthesized MoS2 Wafer-Scale Quality on Fermi Level Pinning in Vertical Schottky-Barrier Heterostructures. *ACS Appl. Mater. Interfaces* **2018**, *10* (46), 39860–39871. https://doi.org/10.1021/acsami.8b13112.

(70) Kaushik, N.; Nipane, A.; Basheer, F.; Dubey, S.; Grover, S.; Deshmukh, M. M.; Lodha, S. Schottky Barrier Heights for Au and Pd Contacts to MoS2. *Appl. Phys. Lett.* **2014**, *105* (11), 113505. https://doi.org/10.1063/1.4895767.

(71) Liu, Y.; Guo, J.; Zhu, E.; Liao, L.; Lee, S. J.; Ding, M.; Shakir, I.; Gambin, V.; Huang, Y.; Duan, X. Approaching the Schottky-Mott Limit in van Der Waals Metal-Semiconductor Junctions. *Nature* **2018**, *557* (7707), 696–700. https://doi.org/10.1038/s41586-018-0129-8.

(72) Wu, L.; Longo, A.; Dzade, N. Y.; Sharma, A.; Hendrix, M. M. R. M.; Bol, A. A.; de Leeuw, N. H.; Hensen, E. J. M.; Hofmann, J. P. The Origin of High Activity of Amorphous MoS2 in the Hydrogen Evolution Reaction. *ChemSusChem* **2019**, *12* (19), 4383–4389. https://doi.org/10.1002/cssc.201901811.

(73) Murthy, A. A.; Stanev, T. K.; Dos Reis, R.; Hao, S.; Wolverton, C.; Stern, N. P.; Dravid, V. P. Direct Visualization of Electric-Field-Induced Structural Dynamics in Monolayer Transition Metal Dichalcogenides. *ACS Nano* **2020**, *14* (2), 1569–1576. https://doi.org/10.1021/acsnano.9b06581.

(74) Hong, S.; Nomura, K. I.; Krishnamoorthy, A.; Rajak, P.; Sheng, C.; Kalia, R. K.; Nakano, A.; Vashishta, P. Defect Healing in Layered Materials: A Machine Learning-Assisted Characterization of MoS2 Crystal Phases. *J. Phys. Chem. Lett.* **2019**, *10* (11), 2739–2744. https://doi.org/10.1021/acs.jpclett.9b00425.

(75) Guo, Y.; Liu, D.; Robertson, J. 3D Behavior of Schottky Barriers of 2D Transition-Metal Dichalcogenides. *ACS Appl. Mater. Interfaces* **2015**, *7* (46), 25709–25715. https://doi.org/10.1021/acsami.5b06897.

(76) Murali, K.; Dandu, M.; Watanabe, K.; Taniguchi, T.; Majumdar, K. Accurate Extraction of Schottky Barrier Height and Universality of Fermi Level De-Pinning of van Der Waals Contacts. *Adv. Funct. Mater.* **2021**, *31* (18), 202010513. https://doi.org/10.1002/adfm.202010513.

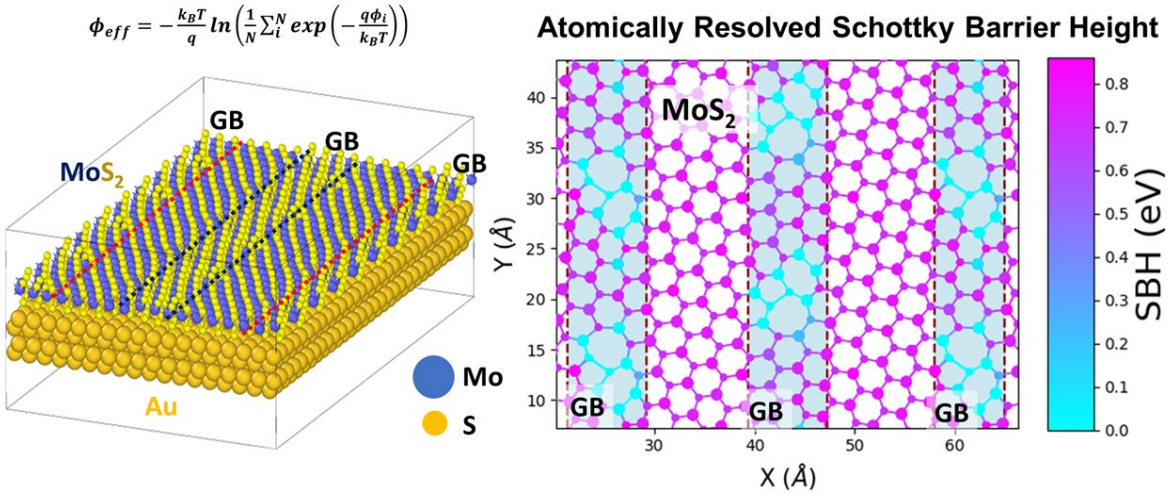

TOC: Graphical Abstract